# 2nd Advanced Optical Metrology Compendium

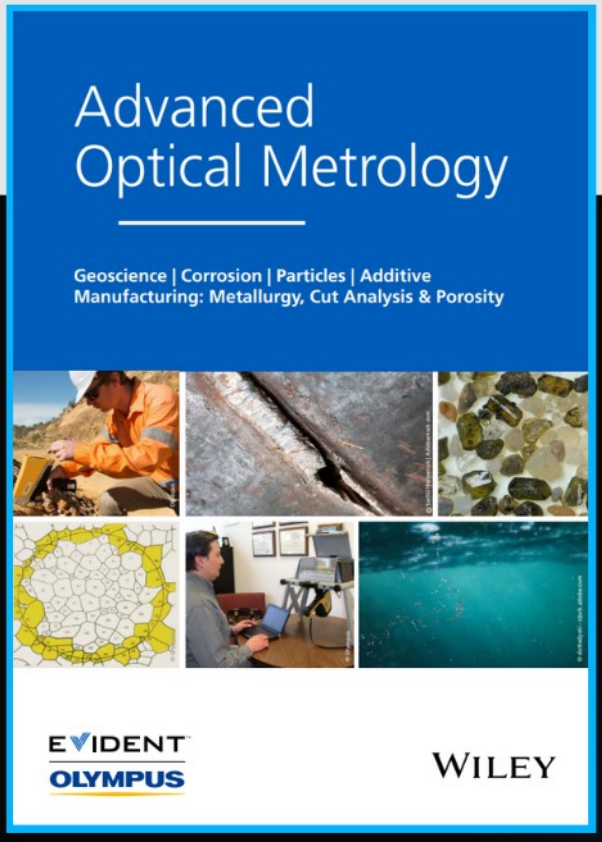


**The latest eBook from Advanced Optical Metrology. Download for free.**

This compendium includes a collection of optical metrology papers, a repository of teaching materials, and instructions on how to publish scientific achievements.

With the aim of improving communication between fundamental research and industrial applications in the field of optical metrology we have collected and organized existing information and made it more accessible and useful for researchers and practitioners.

EVIDENT
OLYMPUS

WILEY

ADVANCED FUNCTIONAL MATERIALS
www.afm-journal.de

# Composition-Dependent Morphology, Structure, and Catalytical Performance of Nickel–Iron Layered Double Hydroxide as Highly-Efficient and Stable Anode Catalyst in Anion Exchange Membrane Water Electrolysis

*Wulyu Jiang, Alaa Y. Faid, Bruna Ferreira Gomes, Irina Galkina, Lu Xia, Carlos Manuel Silva Lobo, Morgane Desmau, Patrick Borowski, Heinrich Hartmann, Artjom Maljusch, Astrid Besmehn, Christina Roth, Svein Sunde, Werner Lehnert, and Meital Shviro**

**Water splitting is an environmentally friendly strategy to produce hydrogen but is limited by the oxygen evolution reaction (OER). Therefore, there is an urgent need to develop highly efficient electrocatalysts. Here, NiFe layered double hydroxides (NiFe LDH) with tunable Ni/Fe composition exhibit corresponding dependent morphology, layered structure, and chemical states, leading to higher activity and better stability than that of conventional NiFe LDH-based catalysts. The characterization data show that the low overpotentials (249 mV at 10 mA $cm^{-2}$), ultrasmall Tafel slopes (24 mV $dec^{-1}$), and high current densities of $Ni_3Fe$ LDH result from the larger fraction of trivalent $Fe^{3+}$ and the optimized local chemical environment with more oxygen coordination and ordered atomic structure for the metal site. Owing to the active intermediate species, Ni(Fe)OOH, under OER conditions and a reversible dynamic phase transition during the cycling process, the $Ni_3Fe$ LDH achieves a high current density of over 2 A $cm^{-2}$ at 2.0 V, and durability of 400 h at 1 A $cm^{-2}$ in a single cell test. This work provides insights into the relationship between the composition, electronic structure of the layer, and electrocatalytic performance, and offers a scalable and efficient strategy for developing promising catalysts to support the development of the future hydrogen economy.**

## 1. Introduction

Due to the increasing energy demand for modern human life and severe environmental pollution, renewable and clean energy is urgently needed. Hydrogen, whose combustion product is only water, is an ideal alternative to natural fuels.[1,2] Moreover, by splitting water into hydrogen and oxygen, water electrolysis is considered as the most feasible technology for producing high purity hydrogen and transportation and storage of clean energy.[2–4] However, water electrolysis generally suffers from sluggish kinetics of the oxygen evolution reaction (OER), which involves a four-electron transfer process that is considered a bottleneck with a non-negligible overpotential.[5,6] Therefore, designing and developing highly effective electrocatalysts to accelerate the OER process is essential.[4,6–8] Transition-metal catalysts, including oxides, hydroxides, sulfides, and

W. Jiang, I. Galkina, L. Xia, W. Lehnert, M. Shviro
Institute of Energy and Climate Research—Electrochemical Process Engineering (IEK-14)
Forschungszentrum Jülich GmbH
52425 Jülich, Germany
E-mail: m.shviro@fz-juelich.de

W. Jiang, I. Galkina, L. Xia, W. Lehnert
Faculty of Mechanical Engineering
RWTH Aachen University
52056 Aachen, Germany

The ORCID identification number(s) for the author(s) of this article can be found under https://doi.org/10.1002/adfm.202203520.



**DOI: 10.1002/adfm.202203520**

A. Y. Faid, S. Sunde
Department of Materials Science and Engineering
Norwegian University of Science and Technology
Trondheim N-7491, Norway

B. F. Gomes, C. Roth
Electrochemical Process Engineering
University of Bayreuth
95447 Bayreuth, Germany

C. M. S. Lobo
Institut für Technische Chemie
Universität Stuttgart
Pfaffenwaldring 55, 70174 Stuttgart, Germany

M. Desmau
Deutsches Elektronen-Synchrotron (DESY)
Notkestraße 85, 22607 Hamburg, Germany

P. Borowski, A. Maljusch
Evonik Operations GmbH
Rellinghauser Strasse 1–11, 45128 Essen, Germany

phosphides, etc., have attracted remarkable attention because of their high natural abundance and OER performance. Among them, layered double hydroxide (LDH) is the most active and promising due to its unique lamellar structure, which allows the active sites to be fully and uniformly exposed to participate in the reaction.[9–12] Especially the NiFe-based LDH has exhibited the leading intrinsic OER activity among the various transition metal LDH catalysts with a rational chemical composition of Ni and Fe.[13–16] To further optimize the OER activity of NiFe LDH catalysts, a variety of approaches have been recently pursued, especially coupling them with other materials. For example, NiFe LDHs integrated with carbon-based materials, including carbon nanotubes, defective graphene, and reduced graphene oxides, etc., or other substrates such as FeNi foil, have achieved superior OER performance.[17–21] The synergistic interaction between NiFe LDH and the integrated nanohybrid could not only contribute to the high electrical conductivity but also enhance the electron and ion transfer within the layer by improving electron coupling at the interface.[13,17,21,22] In addition, studies have aimed to increase the electrochemical surface area and active sites of NiFe LDHs through size control, morphology design,[23,24] and introduction of defects and vacancies in certain specific systems.[14,25] The Fe-dependent OER activity of NiFe LDH has also been reported,[13,15] however, it is not clear whether the modulation of atomic ratio of Ni/Fe would affect the size, morphology, crystallinity, and electronic structure of NiFe LDHs. Meanwhile, despite the evident and desired promotion on OER activity of LDHs, the underlying influence of this strategy on temporal stability, another crucial parameter for commercial application, is still hardly addressed.[15,26]

In addition, the development of anion exchange membrane (AEM) electrolyzers has recently attracted more attention, while their efficiency and practicality, especially for a membrane electrode assembly, fabricated by non-precious metal catalysts, remains to be improved.[27–29] Several latest works have reported performance breakthroughs of AEM with non-noble-metal catalysts: the electrolyzer with NiFeCo cathode and NiFeOx anode reached 1 A $cm^{-2}$ at 1.90 V in 1 M KOH at 60 °C,[30] while a Fe-NiMo-$NH_3/H_2$‖NiMo-$NH_3/H_2$ cell reached a voltage of 1.57 V at 1 A $cm^{-2}$ at 80 °C.[31] The most efficient electrolyzer, using nanometer-sized NiFe-LDH as an anode, Pt/C as cathode, delivers 1 A $cm^{-2}$ at 1.59 V at 80 °C in 1 M KOH.[32] However, these non-noble metal catalysts are obtained in a relatively complicated process, either at high temperature (550 °C)[31] or over a long period (a few days) with the addition of organic solvents,[32] which limits their practicality given the scale and economic cost of catalysts.

In this work, we used a simple precipitation method to tune the composition and structure of NiFe LDHs via the input ratio of the precursor. NiFe LDHs with different Ni/Fe ratios exhibit composition-dependent layers, crystallinity, and local electronic environments of the metal sites, and thus also show differing OER performance. The Ni enriched $Ni_3Fe$ LDH tends to form ordered multilayer nanosheets and shows higher OER activity outperforming the existing NiFe LDH electrocatalysts. At the same time, the *in-situ* Raman spectrum uncovers its active intermediate and dynamic phase transition during the OER process. Based on the structural characterization and half-cell performance evaluation, we selected $Ni_3Fe$ LDH as anode for water electrolysis, which exhibits higher activity and outstanding long-term durability compared to Ir black-based electrolyzers and most state of art AEM water electrolyzers. Furthermore, the $Ni_3Fe$ LDH meets both high performance (efficiency) and low cost (practicality) requirements, confirming its potential in AEM electrolyzers for future commercial applications.

## 2. Results and Discussion

### 2.1. Preparation and Characterization of NiFe LDHs

The NiFe LDHs with different proportions of Ni and Fe (crystal structure illustrated in **Figure 1**) were synthesized by a precipitation method (illustrated in Figure S1, Supporting Information). By controlling the ratio of Ni and Fe precursors, the precipitated hydroxides lead to the formation of three NiFe LDHs. The compositions of $Ni_3Fe$ LDH, $Ni_3Fe_2$ LDH, and $NiFe_3$ LDH were verified by energy-dispersive X-ray spectroscopy (EDX) in the scanning electron microscope (SEM), and inductively coupled plasma-optical emission spectrometry (ICP-OES) analysis (Table S1 and Figure S2, Supporting Information). The X-ray diffraction (XRD) pattern of $Ni_3Fe$ LDH (**Figure 2**a, green curve) exhibits the same Bragg reflections as traditional NiFe LDH, with clear peaks at 11° and 22°, corresponding to the characteristic (003) and (006) planes (JCPDS#40-02 NiFe LDH) of the layered structure in the *c*-axis.[9,33] As the ratio of Fe/Ni increases, the relative peak intensity of (003) and (006) planes diminish in $Ni_3Fe_2$ LDH (Figure 2a, orange curve) and almost disappear in $NiFe_3$ LDH (Figure 2a, red curve). This trend occurs due to the changes of geometric structure, agreeing well with the literature that the absence of (00n) peaks in the XRD patterns evidences the successful exfoliation of multilayers into monolayers.[9,14,34,35]

Subsequently, the composition-dependent structures of these NiFe LDHs were further demonstrated by Raman spectra (Figure 2b). The Raman signal of the $Ni_3Fe$ LDH shows representative bands at 447, 520, and 699 $cm^{-1}$, attributed to the lattice vibrations of the brucite-like LDH structure.[22,36] There is a sharp peak at 1065 $cm^{-1}$, corresponding to the vibrational mode of the intercalated anions in the layers.[37,38] The sharp bands at ≈3650 $cm^{-1}$ are attributed to the hydroxyl stretching vibrations.[39] However, the other two NiFe LDHs show decreasing Raman signals in these two regions, confirming their distinct layered structure: multilayer nanosheets in $Ni_3Fe$ LDHs provide space for the anions, hydroxyl, and/or water molecules to intercalate, while these groups are hardly retained in the single layer $NiFe_3$ LDHs after careful washing during the synthesis process. In short, the results of Raman and XRD measurements are in good agreement and confirm the interaction between the composition and structure of NiFe LDHs.

In addition, X-ray photoelectron spectroscopy (XPS) was used to investigate the influence of composition and structure on

H. Hartmann, A. Besmehn
Central Institute for Engineering
Electronics and Analytics—Analytics (ZEA-3)
Forschungszentrum Jülich GmbH
52425 Jülich, Germany

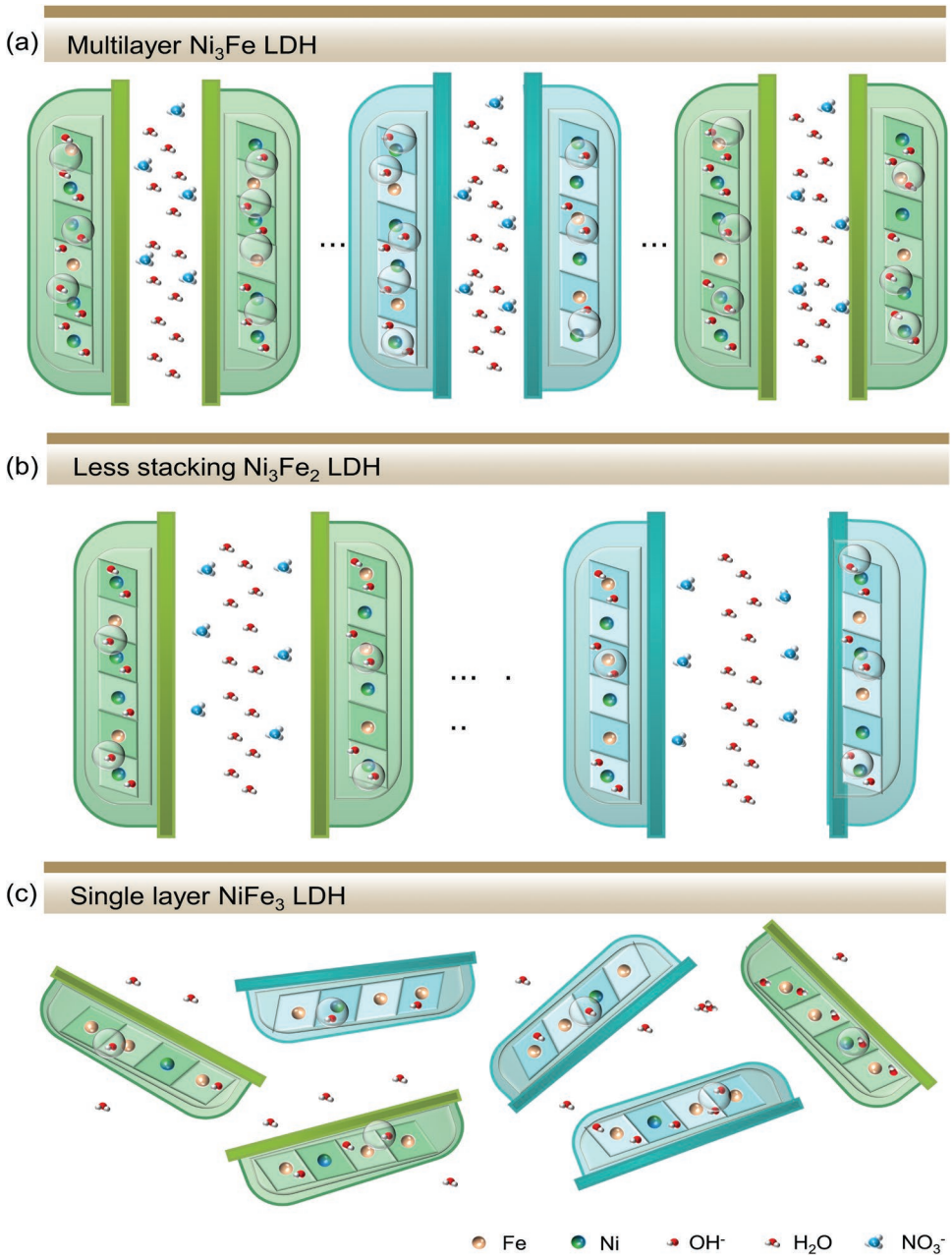


**Figure 1.** Schematic illustration of the crystal structure of NiFe LDHs. a) multilayer $Ni_3Fe$ LDH, b) less-stacking layer $Ni_3Fe_2$ LDH, and c) single layer $NiFe_3$ LDH.

the electronic states of NiFe LDHs. The XPS survey spectrum (Figure S3a, Supporting Information) confirms the presence of C, N, O, Ni, and Fe, the atomic ratio (Table S2, Supporting Information) showing similar oxygen content, and a consistent trend of Fe/Ni ratio as detected by EDX and ICP. The core level Fe 3p region was investigated because it is complicated to correctly analyze the Fe 2p region due to the high-spin configuration of Fe and Ni species.[40,41] The Fe 3p region of NiFe LDHs (Figure 2c) was deconvoluted into two signals with binding energies of 55.8 and 57.2 eV, corresponding to $Fe^{2+}$ and $Fe^{3+}$, respectively. Interestingly, the Fe 3p spectra for $Ni_3Fe$ LDH shifted to higher binding energy by ≈0.5 eV, compared to that of $NiFe_3$ LDH. This shift is likely due to the altered local electronic structure of Fe cations in NiFe LDHs, as confirmed by the $Fe^{2+}$ and $Fe^{3+}$ content (Figure 2e; Table S3, Supporting Information). Compared to $Ni_3Fe$ LDH, more Fe ions in $Ni_3Fe_2$ LDH and $NiFe_3$ LDH are located in the low valence $Fe^{2+}$, rather than $Fe^{3+}$. In contrast, the Ni 2p XPS spectrum (Figure S3b, Supporting Information) of these NiFe LDHs does not show peak shift, and all the deconvoluted peaks agree well with the presence of $Ni^{2+}$.[40] Therefore, there is no obvious charge transfer effect from Fe to Ni. The gradually reduced chemical state of

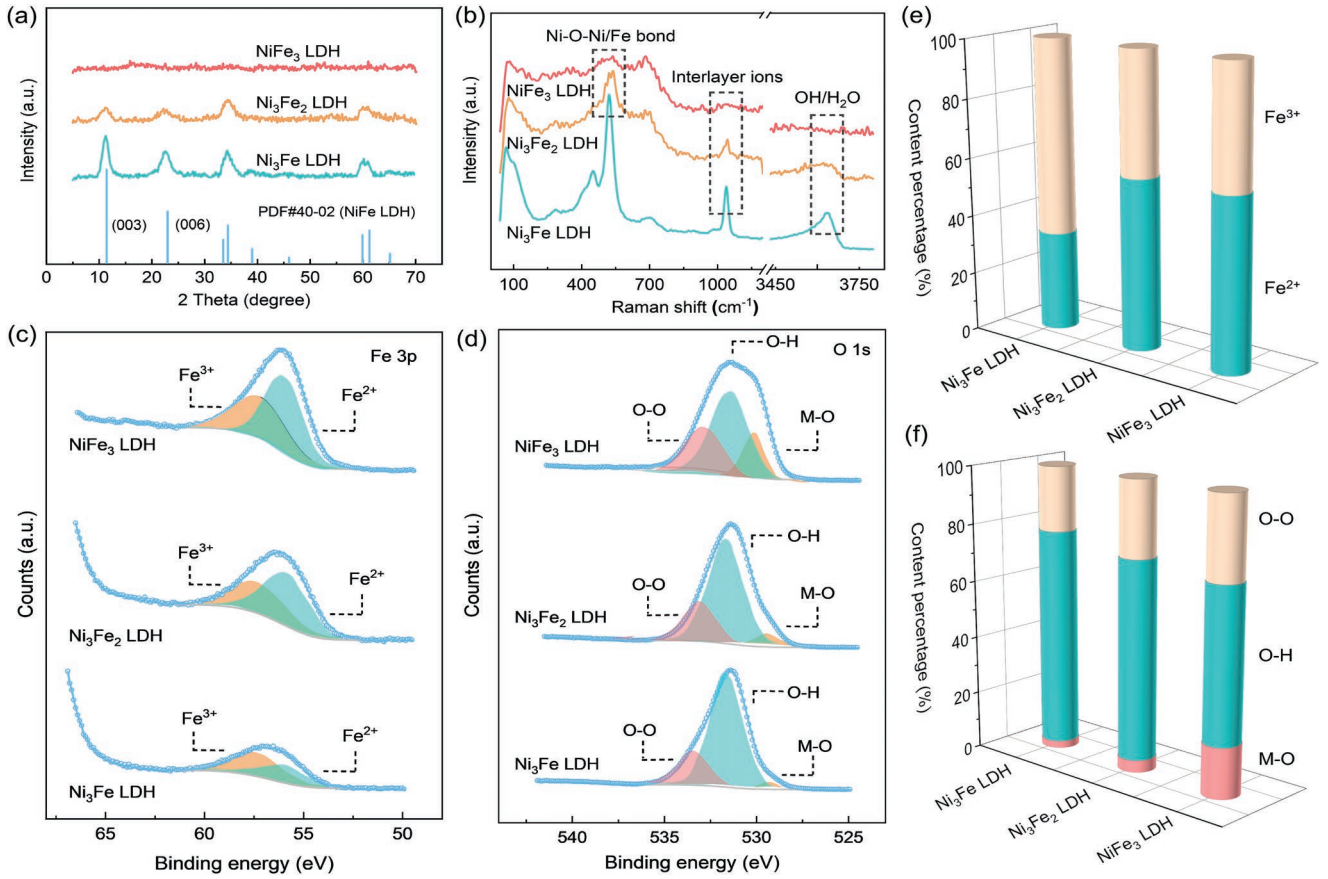


**Figure 2.** Structural characterizations of the NiFe LDH catalysts. a) XRD patterns, b) Raman spectra, c) Core-level Fe 3p, and d) O 1s XPS spectra. e–f) Corresponding Fe and O content (%) in NiFe LDHs calculated from (c) and (d).

Fe is probably due to the oxygen vacancies in the environment of Fe,[42,43] and the existence of $Fe^{2+}$ in NiFe LDH due to the precipitation of $Fe^{3+}$ has also been described in previous works.[44] The gradually widening O 1s XPS spectra indicates the overlap of various O species with each other, and the peaks at 529.0, 531.2, and 533.2 eV are assigned to the metal–oxygen (M—O), O—H hydroxide, and adsorbed O—O bonds in LDH, respectively.[45] The content of each species (Figure 2f and Table S4, Supporting Information) indicates an increased amount of M—O and O—O bonds, as well as a significantly decreased amount of O—H bonds, is observed as more Fe is incorporated into NiFe LDHs, demonstrating weakened binding strength to the active intermediates. This agrees well with the obvious signals of interlayer $OH/H_2O$ for $Ni_3Fe$ LDH from the Raman spectrum.

The morphologies and structures of these NiFe LDH nanosheets were observed by transmission electron microscopy (TEM) in **Figure 3**a–c. $Ni_3Fe$ LDH shows both stacked layers (marked by the yellow arrows) as well as in-plane sheet growth, while $Ni_3Fe_2$ and $NiFe_3$ LDHs are mostly structured as monolayers, despite being produced using the same exfoliation process. The high-resolution TEM (HRTEM) of $Ni_3Fe$ LDH (Figure 3d) indicates that the as-prepared nanosheets exhibit a thickness of 2–4 nm, corresponding to 3–6 LDH layers. The inset of Figure 3d reveals the layer spacing of $Ni_3Fe$ LDH at 0.8–1.0 nm, higher than the theoretical value due to the intercalated $NO_3^-$ anions and $H_2O$ molecular, which is also consistent with previous work.[35,46,47] The enlarged HRTEM image (Figure 3e) reveals the good crystallinity of the nanosheets, clear lattice fringes at 1.5 and 2.5 Å, and the corresponding Fourier-transformed diffraction pattern agrees well with the (110) and (100) planes of NiFe LDH rhombohedral structure in the <001> zone axis. By contrast, the HRTEM image of $NiFe_3$ LDH does not show any lattice fringes, combined with barely recognizable diffraction spots (inset in Figure 3f), together demonstrating its more disordered amorphous structure. The high angle annular dark-field scanning transmission electron microscopy (HADDF-STEM) images and corresponding EDX elemental mapping of $Ni_3Fe$ LDH (Figure 3g) confirm its multilayered structure and the homogeneous distribution of Ni and Fe in the nanosheets. Meanwhile, Ni and Fe are also uniformly distributed in $Ni_3Fe_2$ LDH and $NiFe_3$ LDH as shown by elemental mapping (Figure S4, Supporting Information). This proves that the composition-dependent layered structure and crystallinity of NiFe LDHs are not due to element segregation or phase separation, but have other causes, such as the modulation of metal sites in different chemical environments.

Furthermore, X-ray absorption spectroscopy (XAS) was used to confirm the local structure around Ni and Fe in the NiFe LDH samples. The X-ray absorption near edge structure (XANES)

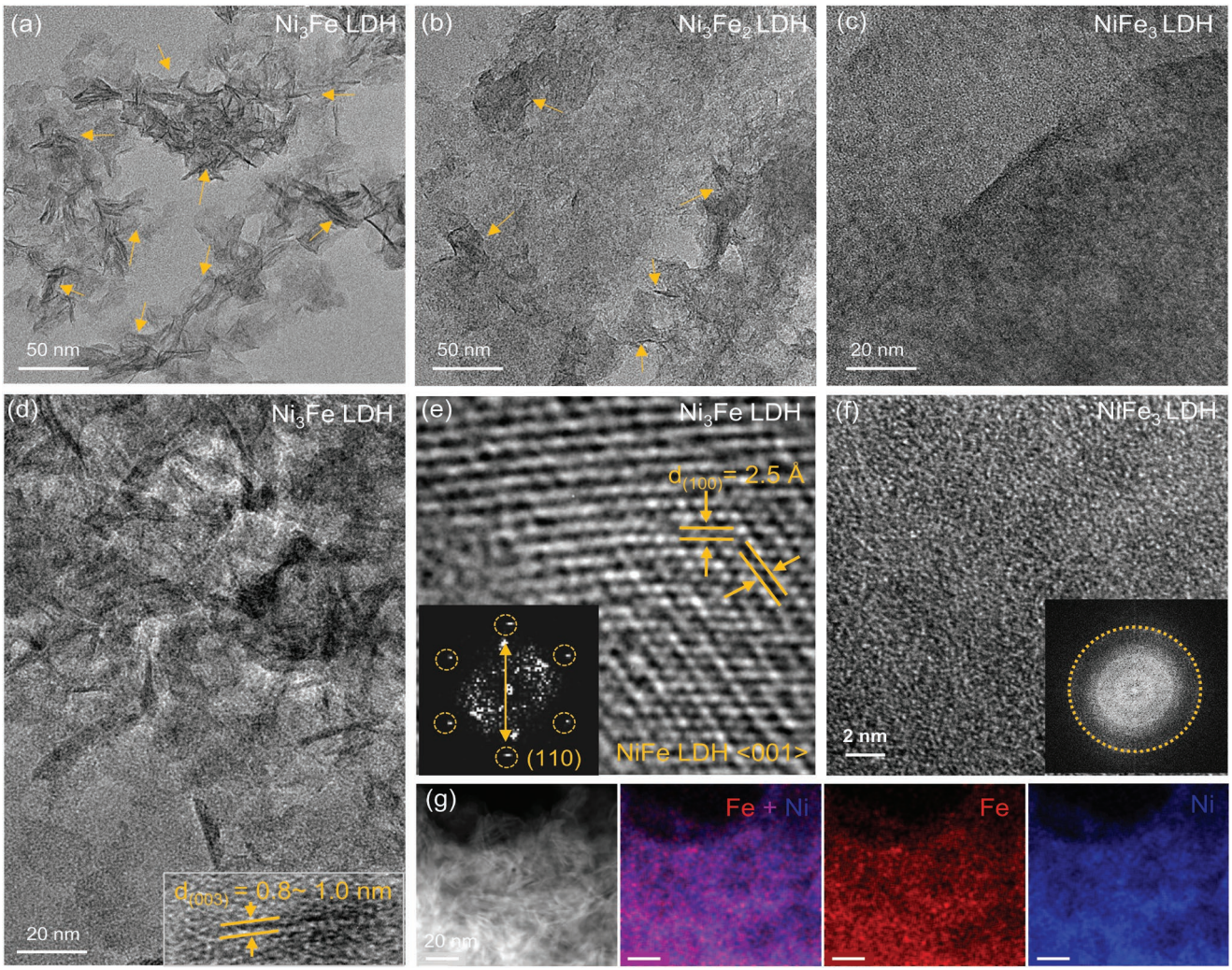


**Figure 3.** Microscopy investigation of the NiFe LDH catalysts. a–c) TEM images of the $Ni_3Fe$, $Ni_3Fe_2$ and $NiFe_3$ LDHs (stacked LDH layers are marked by yellow arrows). d–f) High-resolution TEM images of $Ni_3Fe$ LDH and $NiFe_3$ LDH. The inset of (d) shows the basal spacing of LDH layers. e–f) The insets show the Fourier transform of the region. g) HADDF STEM image and corresponding elemental mapping of $Ni_3Fe$ LDH.

spectra of Fe and Ni K-edge are compared in **Figure 4**. The Fe white line position in $Ni_3Fe$ LDH shifts to higher energy compared to the $Ni_3Fe_2$ and $NiFe_3$ LDH (inset in Figure 4a), which can be associated with an increase in the oxidation state from $Fe^{2+}$ to $Fe^{3+}$. Similarly, the increasing intensity of the white line in $Ni_3Fe$ LDH is also associated with a higher oxidation state, with the $NiFe_3$ LDH showing the least intense white line among the three catalysts. The variation of the Fe oxidation states in the NiFe LDHs, as revealed by the white line shift and intensity, agrees well with the XPS analysis. However, no significant changes in the energy position and intensity were observed for the Ni K-edge of the NiFe LDHs (Figure 4b), indicating that all three NiFe LDHs contain Ni in the same oxidation states, which also agrees well with their similar Ni 2p XPS spectra.

The corresponding Fourier transform (FT)$\chi$(k) of Ni and Fe extended X-ray absorption fine structure (EXAFS) spectra are shown in Figure 4c,d while the parameters obtained with the EXAFS fits are shown in Table S5 and Figure S5 (Supporting Information). The local structure parameters derived from the EXAFS curves and fitting show no significant variations are obtained in the bond lengths around both Ni and Fe centers ($R_{Fe\text{-}O}$ and $R_{Ni\text{-}O}$). The $Ni_3Fe$ LDH shows the highest coordination number (CN) for oxygen surrounded Fe, while the CN of Fe in $NiFe_3$ LDH is the lowest. Therefore, it can be stated that $CN_{Fe\text{-}O}$ reduces with increasing Fe concentration in the NiFe LDHs. The unsaturated oxygen coordination leads to the decreased chemical states of Fe, as revealed by XPS analysis. For the Ni K-edge, $CN_{Ni\text{-}O}$ does not show statistically significant differences, which agrees with almost overlapping spectra and the similar oxidation states observed in XANES. Meanwhile, the Debye–Waller factor ($\sigma^2$) can provide an additional evidence for the structural disorder in the NiFe LDHs. The Debye–Waller factor of the Fe—O shell for the $Ni_3Fe_2$ LDH (0.0088) and $NiFe_3$ LDH (0.0101) is larger than the one for $Ni_3Fe$ LDH (0.0061) (Table S5, Supporting Information), suggesting distorted octahedral Fe—O environment as the composition and layered structure changes. The specific role of Ni and Fe in the synthesis process and structure correlation of NiFe LDH is worth

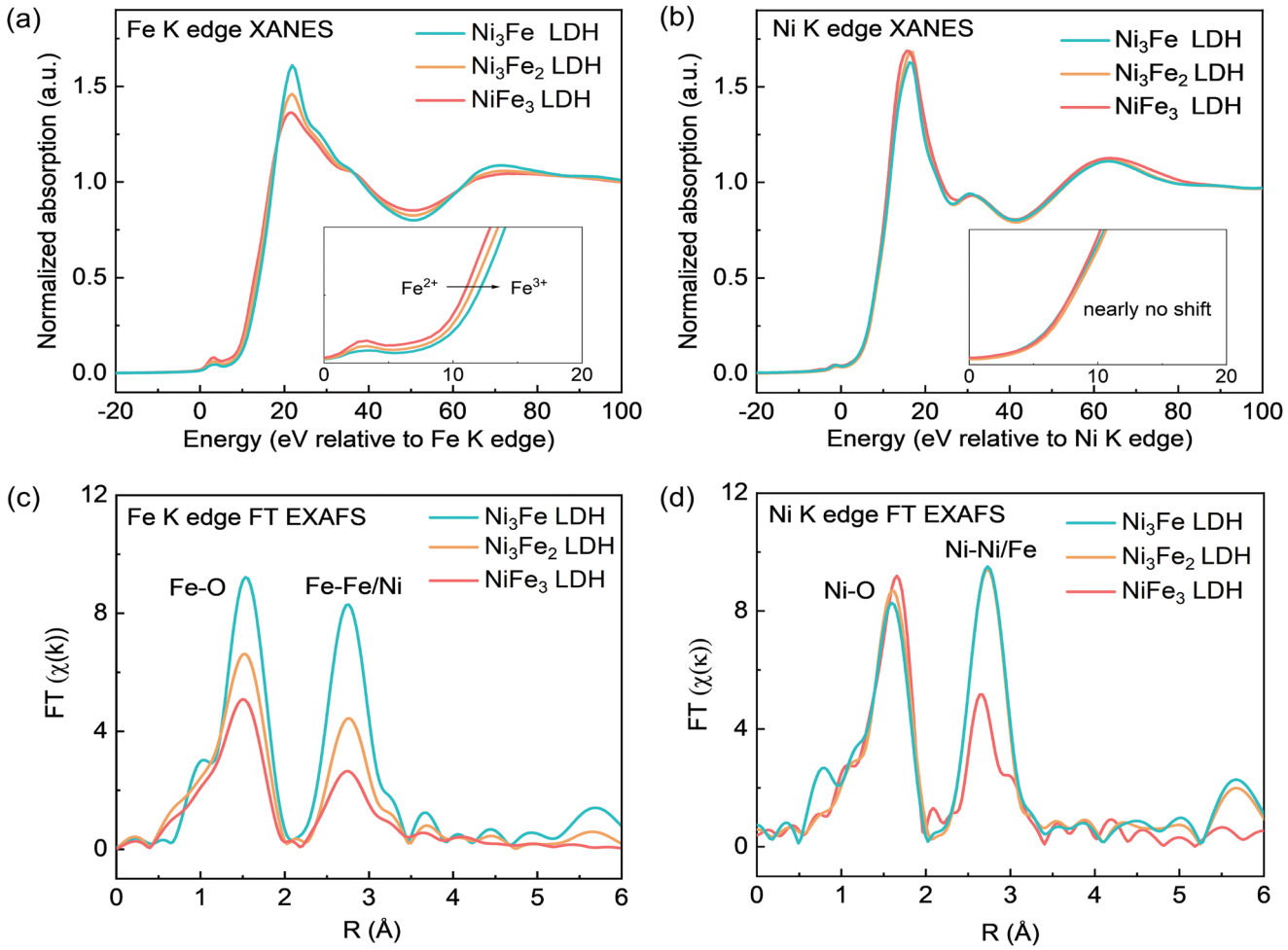


**Figure 4.** XAS spectra of the NiFe LDH catalysts. Normalized XANES spectra of a) Fe K-edge and b) Ni K-edge of NiFe LDHs. EXAFS r-space spectra of the c) Fe K edge and d) Ni K-edge of NiFe LDHs. The R-space spectra were Fourier-transformed from Ni and Fe K-edge $k^3$-weighted EXAFS spectra (in the supporting Figure S5, Supporting Information).

discussing. According to the previous work on the growth mechanism of NiFe LDH, Fe is gradually substituted into the Ni host matrix.[42,48,49] The formation of NiFe LDH starts with the precipitation of FeOOH, which is due to the lower solubility product of $Fe^{3+}$ with $OH^-$ ($1.1 \times 10^{-36}$) compared to that of $Ni(OH)_2$ ($5.48 \times 10^{-16}$). Then, FeOOH diffuses into the $\alpha$-$Ni(OH)_2$ and substitutes nickel sites, and the NiFe LDH phase eventually forms. Therefore, NiFe LDH shows higher structural disorder of NiOOH with increasing Fe content, which is also consistent with previous reports.[15,36,50] But in the structure of mixed metal hydroxides, the Ni and Fe interact with each other so it is difficult to decouple their roles specifically. However, by combining the results of XRD, TEM, XPS, and XAS, we were able to deduce the mechanism of composition-dependent structural changes: When the Fe/Ni ratio increases in NiFe LDHs, the gradually unsaturated oxygen coordination number leads to a distorted Fe—O octahedron, resulting in more disordered amorphous nanocrystals in the $NiFe_3$ LDH. Meanwhile, the lower amount of $Fe^{3+}$ in the $NiFe_3$ LDH nanosheet matrix weakens the interlayer hydrogen bonds, the main connection of multilayers for LDH structure, and leads to a monolayer LDH.

### 2.2. OER Performance of NiFe LDHs

The electrocatalytic OER activity of the three NiFe LDHs was then investigated by linear sweep voltammetry (LSV) in 1 M KOH using a three-electrode system (Experimental Section). $Ni_3Fe$ LDH shows a much lower onset potential and higher OER current compared to $NiFe_3$ and $Ni_3Fe_2$ LDH (**Figure 5**a). The OER activity of NiFe LDH with more Ni was also tested, which did not exhibit superior performance (Figure S6a, Supporting Information). This trend indicates a volcano-type correlation between the Ni/Fe ratio and OER activity of mixed NiFe (oxy)hydroxides, consistent with previous findings. To avoid the Ni redox region, the overpotentials at a current density of 50 mA $cm^{-2}$ were chosen to compare the OER activities of these LDHs (inset in Figure 5a) It is only 287 mV for the $Ni_3Fe$ LDH, and it increased by 60 mV for the $NiFe_3$ LDH. The corresponding Tafel slopes (Figure 5c) of the $Ni_3Fe$ LDH (24 mV $dec^{-1}$) are also smaller than that of $Ni_2Fe_3$ LDH (39 mV $dec^{-1}$) and $NiFe_3$ LDH (43 mV $dec^{-1}$). To avoid the possible influence of the nickel oxidation peak on the Tafel slope, the negative scans of all NiFe LDHs are also compared in Figure S6a (Supporting Information). The similar values in

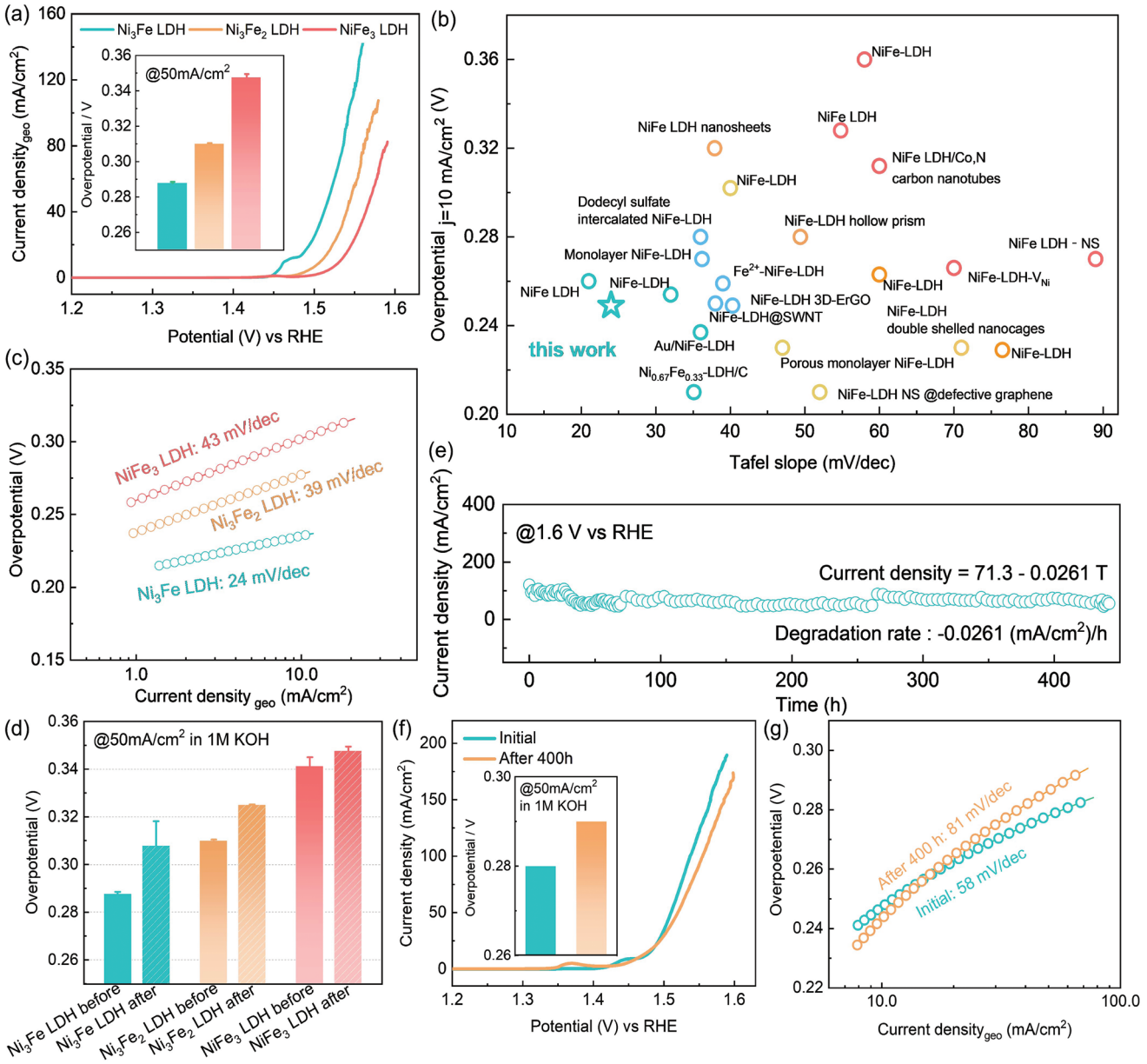


**Figure 5.** Electrochemical behavior of the NiFe LDH catalysts. a) Polarization curves of NiFe LDHs coated on glassy carbon electrode with loading of 0.2 mg $cm^{-2}$ in 1 M KOH. (Inset figure: the overpotential at 50 mA $cm^{-2}$). Plots with an error bar from three repetitions are shown. b) Summary of various NiFe LDH electrocatalysts and corresponding OER performance by the merit of overpotentials at 10 mA $cm^{-2}$ and Tafel slope. c) Tafel slopes d) Stability test: overpotential changes after 1000 cycles from 1.0–1.7 V with a scan rate of 100 mV $s^{-1}$. e) Potentiostatic stability of the $Ni_3Fe$ LDH catalyst at 1.6 V for over 400 h. (f) Corresponding polarization curve and overpotentials (inset), g) Tafel slope during this process.

Figure S6b (Supporting Information) agree with the results of the positive scans. The lower Tafel slope of the $Ni_3Fe$ LDH indicates easier electron transport and favorable reaction kinetics for high-current OER activity, thus increasing its applicability for water electrolysis in a full cell.[9,13,34] This is in agreement with the lower charge-transfer resistance revealed by electrochemical impedance spectroscopy (EIS) measurements, which show a smaller semicircle in the Nyquist plot for $Ni_3Fe$ LDH than the other $Ni_3Fe_2$ LDH or $NiFe_3$ LDH (Figure S6d, Supporting Information). Moreover, the OER activity of our $Ni_3Fe$ LDH catalyst also compares favorably with most NiFe LDH-based catalysts reported in the literature (Figure 5b; Table S6, Supporting Information).

To investigate the reason for the enhanced OER activity of the $Ni_3Fe$ LDH, the electrochemical surface area (ECSA) of these NiFe LDHs was determined by the electrochemical double-layer capacitance ($C_{dl}$) of the catalysts,[51] obtained from the linear slope of capacitive current versus scan rate in a non-Faradaic potential range (Figure S7a—d, Supporting Information). From $NiFe_3$ LDH to $Ni_3Fe$ LDH, the ECSA is halved, which is attributed to the different structure/crystallinity in LDH, as the amorphous structure usually exposes more active sites than crystalline

samples. It also suggests that the superior activity of $Ni_3Fe$ LDH toward OER does not come from an enlarged ECSA, but rather its higher intrinsic catalytical property, which is evident from the comparison of the specific activity of NiFe LDHs normalized by ECSA in Figure S7e (Supporting Information). Therefore, the correlation between electronic structures and OER activity cannot be ignored. When the elemental ratio of Ni/Fe changes, mutual modulation of metal ions in NiFe LDHs occurs due to the charge transfer effect. This tuning of the active metal site then affects the adsorption energy of reactants, the formation energy of intermediates, and the overall catalytic performance.[52,53] Thus, we conclude that another factor, electronic structure, contributes to the differential OER performances of NiFe LDHs. Recent studies have proposed that high-valent metal species in NiFe-based catalysts are possible OER active sites.[54–57] Here, the distinct chemical states of Fe compared to Ni in the three NiFe LDHs confirm its specific role as the metal active site, and the higher proportion of $Fe^{3+}$ in $Ni_3Fe$ LDH account for its superior OER activity among them. In addition, the different order levels of NiFe LDHs dependent on the Ni/Fe content would also dominate the lattice order of NiOOH under OER potentials, which was proved to affect the OER activity of NiFe oxyhydroxides.[56–58] This might be attributed to the optimization of the adsorption energy of oxygenated intermediates at the reactive sites. It is conceivable that the optimized structures of the Fe sites in NiFe LDH correlate with an optimal degree of disorder of the active intermediate, which would be confirmed by the in situ Raman spectrum at OER in the next section.

The stability of OER catalysts, which plays an even greater role in the industrialization of large-scale water electrolysis, was also investigated for these NiFe LDHs. We recorded and compared their overpotential changes at 50 mA $cm^{-2}$ during 1000 cycles (Figure 5d). All the NiFe LDHs exhibit slightly increased overpotentials after being cycled 1000 times: 21 ± 10, 15 ± 4, and 6 ± 3 mV for $Ni_3Fe$ LDH, $Ni_3Fe_2$ LDH, and $NiFe_3$ LDH, respectively. Therefore, among them, the $NiFe_3$ LDH monolayer is the most stable, which is consistent with the reported effect of a layered structure on OER stability.[26] To clarify the degradation mechanism, we performed SEM observations and ICP analyses of $Ni_3Fe$ LDH after the cycling test. The SEM images (Figure S8, Supporting Information) confirmed the more porous nature of the catalyst remaining on the substrate due to electrochemical tuning at high potential. This was verified by the increased O/Ni ratio and the shifted Ni 2p peak towards higher energy (Figure S9, Supporting Information). More detailed investigations on the possible metal dissolution of NiFe LDHs during the stability test were carried out by the inductively coupled plasma mass spectrometry (ICP-MS) test of electrolytes (1 M KOH) under different conditions (Figure S10 and Table S7, Supporting Information). An electrolyte sample after rinsing the electrode served as a blanket comparison and confirmed that no metal dissolved during this procedure. For the $Ni_3Fe$ LDH, the elevated amount of Ni and Fe ions in the electrolyte indicates slight dissolution of Ni and Fe after the stability test, with a dissolution ratio of 1.5% Ni and 5% Fe, indicating negligible catalyst loss and robust electrochemical performance. In contrast, the $Ni_3Fe_2$ LDH and $NiFe_3$ LDH with lower Ni/Fe ratios exhibit lower catalyst dissolution, which explains their stability tendency. To further investigate the long-term stability of NiFe LDH catalysts for practical application, we also conducted the potentiostatic test of $Ni_3Fe$ LDH at 1.6 V for over 400 h. The current density and polarization curves only show slight degradation, with increased overpotential at 50 mA $cm^{-2}$ and Tafel slope during this process (Figure 5e–g). To investigate the dissolution potential and degradation mechanism, the stability of $Ni_3Fe$ LDH and $NiFe_3$ LDH after 5000 cycles were compared in three sequential potential ranges (Figure S11a, Supporting Information; capacitance range 1.0–1.3 V, nickel redox range 1.3–1.5 V, and OER range 1.5–1.7 V) in Figure S11b–e (Supporting Information). The main degradation range for $Ni_3Fe$ LDH is the OER region with significantly decreased current density and increased overpotential, which is similar to the aforementioned steady-state dissolution reported for other OER catalysts.[59,60] In contrast, the $NiFe_3$ LDH shows only some degradation during cycling in the nickel redox region, which is referred to as transient dissolution, possibly due to the surface reconstruction process. The different degradation regions and dissolution behavior are discussed in more detail in conjunction with the in situ Raman results in the next section.

However, not only the layer structure but also the elemental composition changes of NiFe LDHs may also affect their stability. To clarify the effects of layer structure and elemental composition on the activity and stability, we distinguish these two factors by comparing a series of NiFe LDHs with the same chemical components. The bulk $Ni_3Fe$ LDH was synthesized by excluding the exfoliation process and confirmed by XRD patterns and TEM images (Figures S12 and S13, Supporting Information). Their corresponding overpotentials manifest superior OER activity of exfoliated LDH compared to bulk LDH. This improvement is due to the increased exposure of active sites by peeling stacked nanosheets, as confirmed by the ECSA changes from 3.82 to 6.75 μF $cm^{-2}$ for the exfoliated and bulk LDHs, respectively. Simultaneously, the exfoliated $Ni_3Fe$ LDH also exhibits less current degradation and more stable overpotential at 50 mA $cm^{-2}$ during 1000 cycles, verifying the positive effect from exfoliated LDHs on OER stability. ICP-MS results of the electrolytes confirm that the bulk $Ni_3Fe$ LDH show more Fe dissolution (10.2%) than exfoliated $Ni_3Fe$ LDH (5.0%, revealed in Figure S10, Supporting Information), which is also consistent with its higher degradation during the cycling process. This proves the influence of the layer structure of NiFe LDHs on OER stability. Overall, we compared the NiFe LDHs of the same composition with different layer structures and found that the exfoliation process does not invariably increase the ECSA and OER activity, but it does increase stability.

### 2.3. In Situ Structure Evolution of NiFe LDHs by Raman Spectra

The phase transformation on the surface of NiFe LDH was studied by in situ Raman with the applied overpotential between 1.3 to 1.7 V (**Figure 6**). For $Ni_3Fe$ LDH in the range from 1.3 to 1.5 V, the constant Raman band at 520 $cm^{-1}$ indicates its unchanged phase structure (Figure 6a), while the sharp band at 1060 $cm^{-1}$ results from the absorption of $OH^-$ intermediate layers of LDHs at elevated potentials.[38,61] When the potential reaches 1.6 V, the existing frequencies at 477 and 557 $cm^{-1}$

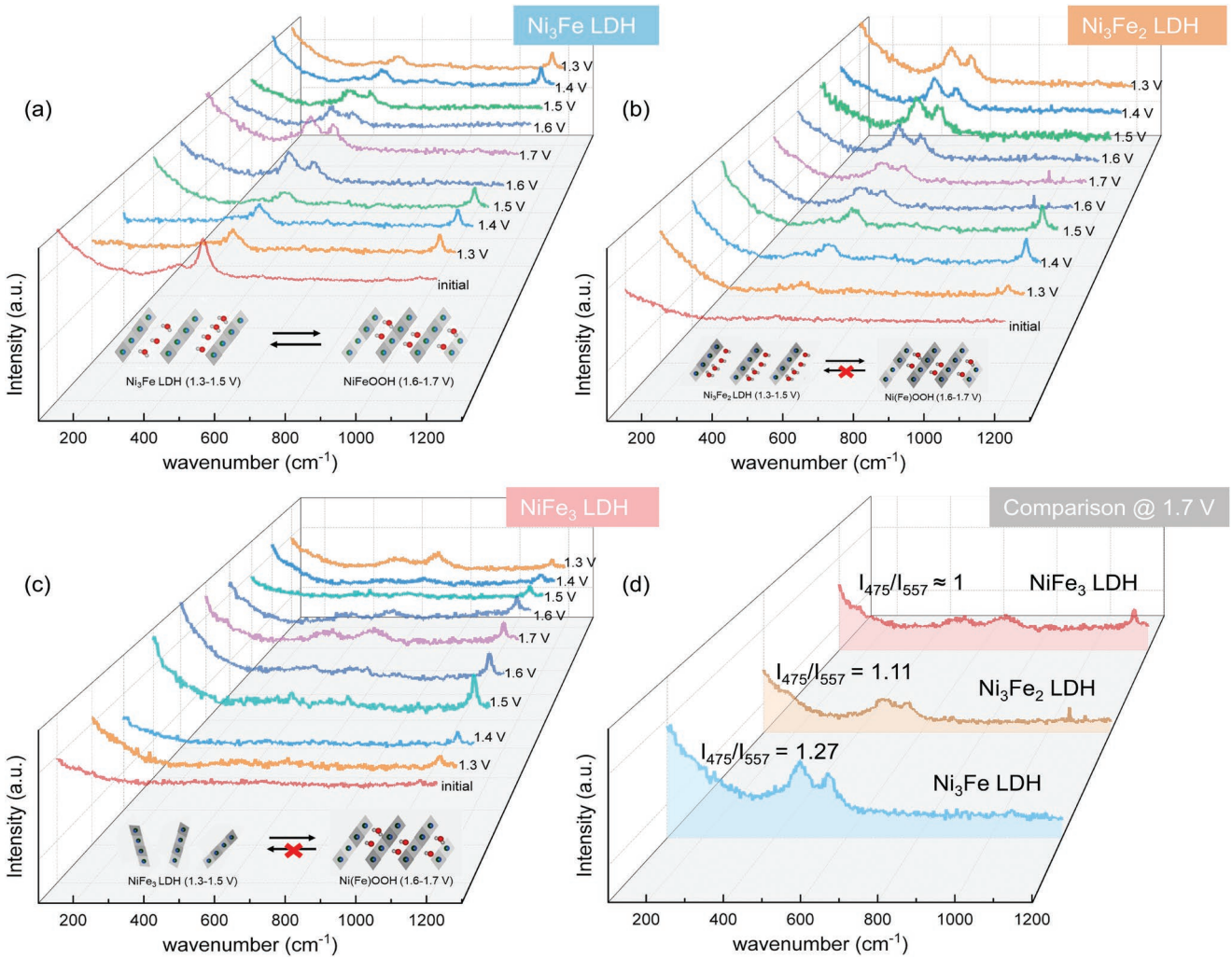


**Figure 6.** In situ Raman spectra of the NiFe LDH catalysts. Spectra were obtained after keeping initial sample at different potentials in sequence: 1.3, 1.4, 1.5, 1,6, 1.7, 1.6, 1.5, 1.4, and 1.3 V. a) $Ni_3Fe$ LDH, b) $Ni_3Fe_2$ LDH and c) $NiFe_3$ LDH. d) Comparison of the Raman band for NiFe LDHs at high potential 1.7 V and the corresponding value of the $I_{475}/I_{557}$ band ratio.

match well with the spectral features of γ-NiOOH, which acts as an active intermediate that is beneficial for high OER reactivity.[61–63] This suggests that the three NiFe LDHs convert to NiFe-oxyhydroxides, so the roles of Ni and Fe may be different compared to the initial states, as we discussed above. However, the actual catalytic sites of these intermediates could not be precisely identified, although some previous works have tried to solve this problem using advanced characterization techniques or theoretical calculations.[56,57,64–68] Even the in situ techniques can verify the oxidation state/electronic structure of Ni/Fe at OER potentials, they can hardly distinguish whether Ni or Fe is the actual active site of NiFe oxyhydroxides. DFT calculations are based on a theoretical structural model that may be far from the actual active intermediates because their detailed structure, e.g., metal site arrangement, termination plane, electron spin state, and adsorbed ions, is largely unknown due to the lack of experimental data. Therefore, the identification of the changes in the oxygenated intermediates is worth for their catalytic activities. In $Ni_3Fe$ LDH, the Raman band at 1060 $cm^{-1}$, attributed to intercalated ions, vanishes at 1.6–1.7 V, indicating the deprotonation of the hydroxyls for active oxygen species under OER conditions.[63,69] In contrast, these species did not exist for $NiFe_3$ LDH, indicating unfavorable bonding energy for reaction due to the higher Fe content. This retained active intermediate species from the rate-limiting step during the OER process also indicates the sluggish dynamic of $NiFe_3$ LDH catalyst (Figure 6b,c).

At the highest potential of 1.7 V, the band intensities of NiOOH reach a maximum at 477 and 557 $cm^{-1}$, but they vary for the three NiFe LDHs (Figure 6d). For quantification, the ratio of absolute band intensities ($I_{475}/I_{557}$) was considered as an important parameter depending on the applied potential.[70] With increasing Fe content, the band intensity at 475 $cm^{-1}$ decreases more than the band at 557 $cm^{-1}$, resulting in a gradually decreasing $I_{475}/I_{557}$ band ratio, which is due to the disorder caused by a larger amount of iron atoms and agrees well with the initial order-level determined by TEM and XAS. The band ratio of $Ni_3Fe$ LDH was reported to be in the optimal interval, while further increased Fe content and disorder in $NiFe_3$ LDH could be unfavorable for OER activity.[50]

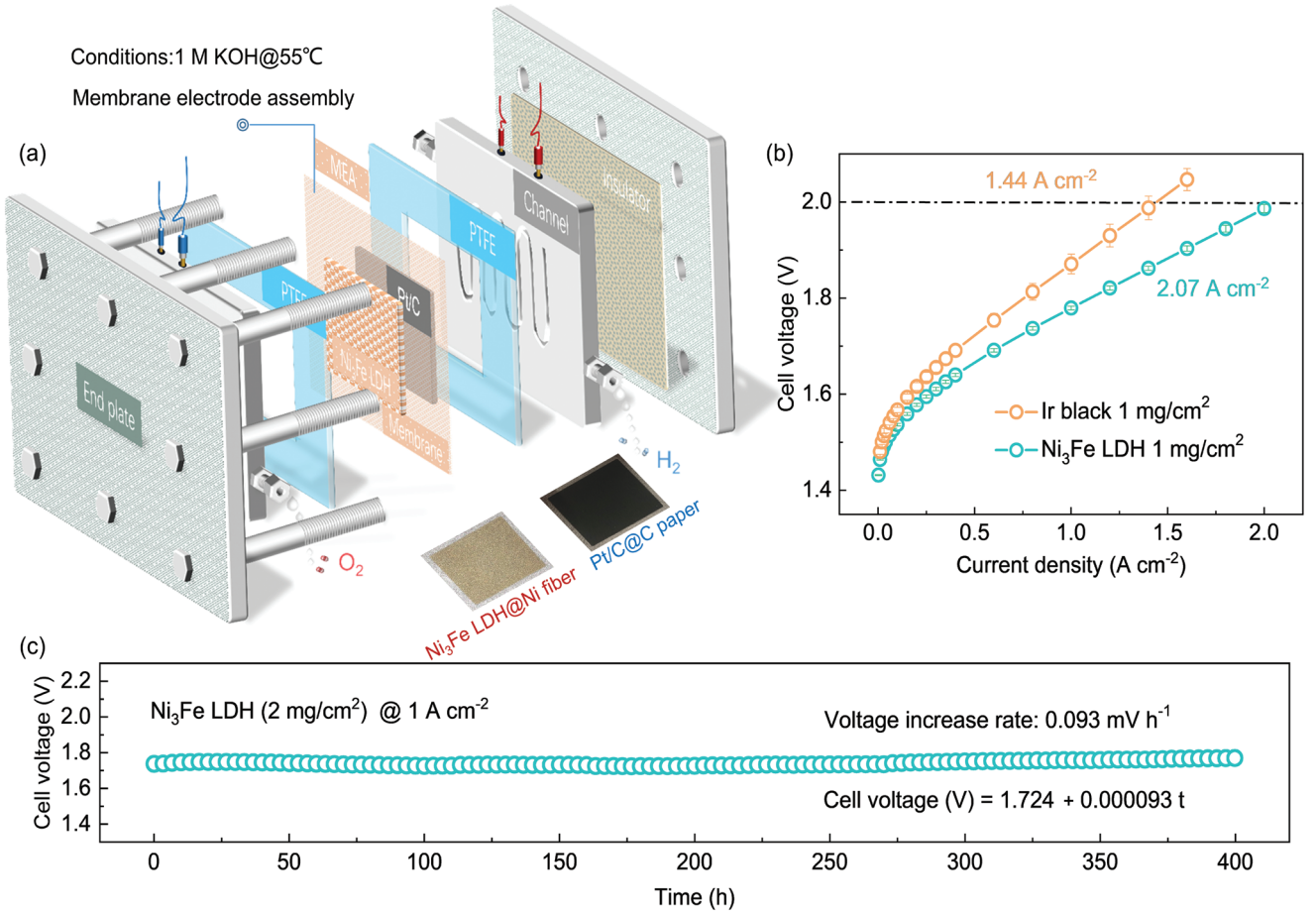


**Figure 7.** Water electrolysis performance of $Ni_3Fe$ LDH catalyst in single cell. a) Schematic illustration of the structure of an electrolyzer cell. b) Polarization curve of water electrolysis comparing the cell based on $Ni_3Fe$ LDH@Ni fiber electrode (green) with commercial Ir black @ Ni fiber electrode (orange) as an anode, respectively, and a commercial Pt/C@ carbon paper electrode as a cathode. c) The cell voltage of the electrolyzer held at 1 A cm$^{-2}$ for ≈400 h in 1 M KOH alkaline solution.

When the potential drops from 1.7 to 1.3 V, the signals of NiOOH species gradually disappear and the Raman bands of LDH phase reappear for $Ni_3Fe$ LDH, consistent with the reduction peak of NiOOH to $Ni(OH)_2$ in the CV curves (Figure S6b, Supporting Information). The in situ Raman spectra show the reversible structure transformation between NiFe LDH and Ni(Fe)OOH during the potential cycling processes. While the Raman bands for $Ni_3Fe_2$ LDH and $NiFe_3$ LDH at 1.3 V are distinct from the initial signals, demonstrating the irreversible structural transformation process. These different phase transition trends during the cycling process could also be related to the structure and OER stability of NiFe LDHs: highly ordered $Ni_3Fe$ LDH have more coordinated oxygen atoms in the Ni/Fe sites, and are, therefore, stable enough for the phase transition process, therefore, only exhibits slight degradation during the cycling in nickel redox region. However, the $NiFe_3$ LDH with a higher disorder degree, and probably poor structural stability, cannot transform back from the intermediate phase anymore, leading to an irreversible dynamic process and corresponding higher metal dissolution during this structural transformation process. This is the main instability mechanism called transition dissolution from surface reconstruction process. Our result established a close relationship between the atomic/electronic structure, dynamic transition process, and OER stability of NiFe LDH catalysts.

### 2.4. AEM Water Electrolysis Measurements

Finally, we would like to point out the practical applications of the NiFe LDH catalyst in terms of activity and long-term stability in a real single cell system (illustrated in **Figure 7**a) for anion exchange membrane (AEM) water electrolysis. A membrane electrode assembly (MEA) with $Ni_3Fe$ LDH@Ni fiber as an anode, Pt/C@ carbon paper as cathode, both manufactured with DURAION ionomer, and DURAION anion exchange membrane from Evonik Industries AG and tested at 55 °C in 1 M KOH. Figure 7b shows the polarization curves of the cell based on $Ni_3Fe$ LDH catalysts compared to the benchmark cell based on Ir black (using the same loading of 1 mg cm$^{-2}$) as an anode.

The $Ni_3Fe$ LDH based cell exhibits a superior performance: a current density of 1 A cm$^{-2}$ was achieved at 1.745 V, while an even higher current density of 2.07 A cm$^{-2}$ was achieved at 2.0 V, in contrast the current density of the Ir-based cell at 2.0 V is only 1.44 A cm$^{-2}$. This single cell performance is also

prevalent when compared to other AEM electrolyzers tested under the same or similar conditions (Table S8, Supporting Information).[71–76] Usually, the non-precious metal catalysts would be used in AEM electrolyzers with a higher loading (such as 2, 3, or 4.8 mg $cm^{-2}$) for performance evaluation,[29,77,78] thus we also compared the $Ni_3Fe$ LDH-based electrolyzers with catalyst loadings of 1 and 2 mg $cm^{-2}$. The polarization curves (Figure S14, Supporting Information) show an increased current density at higher mass loading, but although this increase is not substantial. In the end, we kept the loading of $Ni_3Fe$ LDH catalysts at 2 mg $cm^{-2}$ as default for other tests.

To characterize its stability, the cell was measured under galvanostatic conditions at 1 A $cm^{-2}$ for 400 h. The resulting cell voltage in Figure 7c is stable despite some fluctuations due to bubbles formation. The increase in potential is lower than 0.1 mV $h^{-1}$ as shown by the slope of this curve. Previous work has reported short-term stabilities of several hours to a few days for NiFe-based single cells.[31,32,79–81] In this work, very high performance and a very good operation stability over 400 h were observed. This result indicates the high stability of the MEA prepared with non-PGM $Ni_3Fe$ LDH as anode catalyst, DURAION ionomer, and DURAION anion exchange membrane. The faradaic efficiency and energy conversion efficiency of this MEA were calculated at 1 A $cm^{-2}$ according to reported methods.[31,32,82,83] The produced $O_2$ and $H_2$ gas from the electrolyzer cell were quantified by the water–gas displacement method and compared with theoretical gas volume for the faradaic efficiency (Figure S14, Supporting Information). The amount of $O_2$ collected from the electrolyzer agrees well with the theoretical values, indicating a high utilization rate of electrical energy for water electrolysis with a faradaic efficiency of 97.8%. The corresponding energy conversion efficiency of this MEA at 1 A $cm^{-2}$ is 69.7%, comparable to other reported MEAs even the temperature was relatively low at 55 °C.[32,82] Therefore, NiFe LDH is a greatly promising candidate as the next generation non-noble OER catalysts with high efficiency and durability for practical AEM water electrolyzers.

## 3. Conclusion

In summary, NiFe LDHs were prepared by a facile precipitation method, which results in compositional-dependent morphology, atomic and electronic structure. The correlation between the composition and structure of NiFe LDHs was investigated by XPS, TEM, and XAS. The more Fe is incorporated into LDHs, the lower the proportion of $Fe^{3+}$ and number of coordinated oxygen atoms, while the disorder and the degree of amorphism increase. The multilayer $Ni_3Fe$ LDH shows higher OER activity than the single layer $NiFe_3$ LDH on RDE and also outperforms most reported NiFe LDHs. In situ Raman shows that the dynamic self-constructed Ni(Fe)OOH phase is the actual active species of all NiFe LDHs at the OER potential, while the more disordered $Ni_3Fe_2$ and $NiFe_3$ LDHs show an irreversible phase transition during the potential change, the more ordered $Ni_3Fe$ LDHs is able to return to the initial stage with good crystallinity. In addition, the single cell utilized $Ni_3Fe$ LDH as anode catalysts for alkaline exchange membrane water electrolysis exhibits superior current density compared to its Ir-based counterpart, as well as a robust long-term stability at 1 A $cm^{-2}$ for at least 400 h. Our study provides the detailed characterization and analysis of the catalyst structures, including morphology, layer structure, element valence, coordination environment, and catalytical performance of NiFe LDHs. The reported dominant activity and stability of $Ni_3Fe$ LDH on RDE and single cell make this a promising non-precious metal-based catalyst, moreover, the uncovered mechanism of the mutual correlation between composition and morphology may help to understand and design more highly efficient NiFe LDH or other kinds of catalysts for application in alkaline water electrolyzers.

## 4. Experimental Section

*Materials*: All chemical reagents including $Ni(NO_3)_2$ (nickel (II) nitrate hexahydrate, ACS reagent, ≥98.5%, Sigma Aldrich), $Fe(NO_3)_3$ (ferric nitrate hexahydrate, ACS reagent, ≥98%, Sigma Aldrich), NaOH (sodium hydroxide, gradient grade, ≥99.9%, Honeywell), and KOH (potassium hydroxide, ACS reagent, ≥85.0%, Sigma Aldrich) used without further purification. Deionized water was used in all experiments.

*Synthesis of NiFe LDHs*: A co-precipitate method based on the low solubility product ($K_{sp}$) of metal ions ($Ni^{2+}$ and $Fe^{3+}$) was used in an alkaline solution. 3 mmol of $Ni(NO_3)_2$ and 0.75 mmol of $Fe(NO_3)_3$ were mixed and added into 50 mL of NaOH aqueous solution (0.15 M) under strong stirring at 1000 rpm for 10 min at room temperature around 25 °C. The precipitate was then collected by centrifugation, washed with DI water, and re-dispersed in 25 mL DI water. The exfoliation was implemented by intense ultrasound treatment on IKA Dispersers (ULTRA-TURRAX, IKA-Werke GmbH & Co. KG) for 30 min. Finally, the sample was centrifuged at 4500 rpm for 5 min, cleaned with DI water and ethanol, and dried in a vacuum oven overnight at 25 °C. The resulting $Ni_3Fe$ LDH was collected for further characterizations. To produce the remaining catalysts, the ratio of $Ni(NO_3)_2$:$Fe(NO_3)_3$ was changed to 2.5:1.25 to obtain the $Ni_3Fe_2$ LDH and to 1.875:1.875 to obtain the $NiFe_3$ LDH (the amounts in the ratios are given in mmol).

*Physical Characterization*: The crystal structure was confirmed first by the XRD (D8 Discovery X-ray Diffractometer) using Cu-K$\alpha$ radiation (0.154 nm) in Bragg–Brentano geometry with a $2\theta$ range from 5° to 70°. The morphology and elemental composition were characterized by scanning electron microscopy (SEM, Zeiss Gemini Ultra Plus instrument). Transmission electron microscopy (TEM) images were obtained using a FEI Titan, 80–300 TEM with a $C_s$ corrector for the objective lens (CEOS GmbH).[84] The microscope was operated at 300 kV. Raman spectrum was obtained at the laser wavelength of 532 nm, with power of 0.2 mW. The aperture is fixed at 50 × 1000 µm, and resolution is ≈9–19 $cm^{-1}$, single spectrum is accumulated at integration time of 2 s.

XPS spectra were collected with a Phi5000 VersaProbe II from ULVAC-Phi Inc. with Al K$\alpha$ as the monochromatic source (1.486 keV). The powder samples were pressed into an indium foil fixed with clamps on a sample holder. The survey spectra were obtained at 187.5 eV pass energy, 0.8 eV per step, 100 ms per step while the detailed core-level spectra were recorded with a pass energy of 23.5, 0.1 eV per step. Charge-correction is conducted by setting the peak of C—C 1s to 285 eV.

The iCAP 7600 was used for ICP-OES for powder samples, two aliquots of ≈30 mg per sample were dissolved in 3 mL HCL + 1 mL $HNO_3$ at ambient temperature 25 °C for 0.5 h. Each digestion solution was made up to 50 mL, and 2 replicate dilutions of each digestion solution (100-fold dilution) were prepared and analyzed. ICP–MS: Agilent 7900 was used to measure the electrolytes. For the electrolytes (1 M KOH) under different conditions, 20 mL was picked from the 200 mL total electrolytes after the stability test (1000 cycles between 1.0S–1.7 V). Three replicate dilutions of each sample (100-fold dilution) were prepared and analyzed, then the averaged data with deviation were obtained.

XAS experiments were conducted at the Fe K-edge (7112 eV) and the Ni K-edge (8333 eV) on the P65 beamline of the Deutsches Elektronen-Synchrotron (HASYLAB/DESY PETRA III, Hamburg, Germany).[85] Incoming photon flux energy was modulated with a Si(111) double crystal monochromator and the effective suppression of higher harmonics was achieved using Si-plane mirrors. The data were collected from −150 eV to +1000 (measured against the edge energy) with a scan energy increment of 0.55 eV in continuous mode. Spectra were collected in transmission mode, concomitantly with the spectrum of Fe or Ni foil for energy calibration and alignment.

Three NiFe LDH samples, prepared in pellets to ensure an edge absorption of 1 unit, were analyzed using XAS. A total of four scans were measured and averaged per sample. Fe K-edge and Ni K-edge were measured for all samples and references ($Fe(NO_3)_3$ and $Ni(NO_3)_2$). Oxidation state information was obtained through X-ray absorption near edge structure (XANES) region analysis and structure geometry information (coordination number and bond distance) was determined through the fit of the extended X-ray absorption fine structure (EXAFS). The measured spectra were processed (calibrated, averaged and normalized) using the Athena software and the EXAFS fits were made using the Artemis software.[86]

The XANES region from −20 to 100 eV relative to Fe and Ni K-edges was analyzed. The samples were compared with the spectra of the precursors: $Fe(NO_3)_3$ and $Ni(NO_3)_2$, respectively. The EXAFS spectra were normalized in the range of 150 to 850 eV in relation to the edge, using the Athena program.[86] The normalized spectra were then transferred to the Artemis program,[86] where the fitting was made. The appropriate scattering paths were generated with the atoms code (already present in the Artemis program).[87] The appropriate scattering paths were generated and extracted with the atoms code already embedded in the Artemis program. Only one single-scattering path was used for each edge, Fe—O and Ni—O first shell for Fe K-edge and Ni K-edge, respectively. The fitting was done in R-space (1 to 2 Å). For all fits, the Debye–Waller factor, $\sigma^2$, and $E_0$, which is a parameter used to align data energy with reference material energy, were calculated. The coordination number, $N$, was determined using the "Amp" parameter in the Artemis program, according to the following equation:[88]

$$N = \left(\text{Amp} \times N_{\text{theory}}\right)/S_0^2 \quad (1)$$

where $S_0^2 = 1$ for Fe and Ni K-edges and $N_{\text{theory}}$ (Fe—O and Ni—O) = 6.

A reasonable EXAFS fit takes into account many parameters and their accuracy (as well as correlations): the R-factor should be <0.02 (see Table S1, Supporting Information), $\Delta E_0$ should not be too large (typical range ± (0–15) eV), $S_0^2$ was fixed at 1, as was previously done (typical range 0.7–1.05) and $\sigma^2$ (typical range 0.002–0.03 Å$^2$) cannot be negative,[86] with the number of independent points not larger than 2/3 of the total number of independent point as evaluated by the Nyquist criterion.[89]

*Electrochemical Tests*: Testing setup: The OER performance of the NiFe LDHs was measured in an electrochemical workstation (BioLogic Science Instruments, SP-150) and RDE setup (Pine Research Instrument) using a standard three-electrode cell designed to hold the glassy carbon electrode (GC, $\phi$ = 5 mm, Pine Research), a Pt wire counter electrode, and a Hg/HgO reference electrode (CHI Company). The working electrode was fabricated by depositing catalyst ink on glassy carbon (GC) electrodes.

Preparation of working electrode: mixing 8 mg of catalyst in 1.5 mL isopropanol, 0.5 mL DI-water, and 20 µL DURAION ionomer then sonicated for 40 min. Next 10 µL of the prepared catalyst ink was drop-casted on the GC electrode and dried in air at room temperature. Catalyst loading on the GC surface was kept at 0.2 mg cm$^{-2}$ unless otherwise stated. All the electrochemical measurements were conducted in Ar-saturated 1 M KOH electrolytes, which were then purged with $O_2$ for 20 min before performing the OER experiments, with a rotation speed of 1600 rpm at room temperature (20 ± 2 °C)

Testing protocols: Activation protocol was used before the linear sweep voltammetry (LSV) measurements by cycling the working electrode between 1.0 and 1.7 V versus RHE (iR corrected) at a scan rate of 100 mV s$^{-1}$ for 10 cycles based on the preliminary experimental conclusions. The LSV polarization curves were recorded in a potential range from 1.0 to 1.7 V versus RHE at a sweep rate of 5 mV s$^{-1}$ without iR correction. The potential applied to the ohmic resistance was extracted later manually. Here the iR drop at each electrolyte was compensated at 85% of high-frequency resistance. The cycling stability was measured by LSV curves before and after 1000 cycles between 1.0–1.7 V with a scan rate of 100 mV s$^{-1}$ in 1 M KOH. The long-time chronoamperometry responses were measured at a fixed potential (1.6 V vs RHE) for 20 h in 1 M KOH. The electrochemical impedance spectroscopy (EIS) measurements were performed over the frequency range from 0.01 to$10^5$ Hz at 1.6 V. To determine the NiFe LDH catalysts electrochemical area the original CV curves were scanned at a non-faradic area between 1.1 to 1.2 V by changing the rate from 5, 10, 25, 50, 100, 200, and 400 mV s$^{-1}$ in 1 M KOH. The corresponding capacitance values were obtained by the slope of the linear relationship between current and scan rate. The long-term stability test of NiFe LDH at potentiostatic condition was fixed at 1.6 V for 400 h with 0.2 mg cm$^{-2}$ loading on nickel foam to improve the catalyst dropping from support substrates during the continuous oxygen evolution process as confirmed by previous work..[90] Then the corresponding LSV curves and Tafel slopes are compared to evaluate the degradation.

*In Situ Raman*: In-situ Raman Spectro-electrochemistry of NiFe LDH catalysts was carried out using WITec alpha300 R Confocal device equipped with a 532 nm laser (10 mW power). More details about the setup can be found in previous work.[91,92] The in situ Raman measurements were performed in a Teflon cell with a quartz glass window. The NiFe LDH catalyst ink was deposited on the glassy carbon (GC) electrode. The GC electrode (pine research), a Pt foil, and Hg/HgO (pine research) were used as a working, counter, and reference electrode, respectively. The Hg/HgO reference electrode was calibrated versus RHE in a three-electrode cell using two platinum electrodes (working and counter).[93] The Potential-dependent Raman spectra are acquired after holding at each potential in 1M KOH (semiconductor grade) for 5 min: initial sample, 1.3, 1.4, 1.5, 1,6, 1.7, 1.6, 1.5, 1.4, and 1.3 V. The initial sample is the sample at an open-circuit voltage (OCV). The Raman spectrum acquisition was collected after 10 sweeps of 10 s from 100 to 1200 cm$^{-1}$ and was calibrated using a 520.7 cm$^{-1}$ silicon Raman peak.

*Electrode Fabrication and Test of MEA*: For the MEA cell, the CCS electrode fabrication method was chosen. First, the ink formulation for both catalysts, $Ni_3Fe$ LDH and Pt/C, was found to be optimal as follows: the catalyst powder and ionomer were dispersed for 5 min in a mixture of ethanol and water (1:1) with a rotating ultraturrax followed by 30 min of ultrasonic finger treatment. The catalyst ink was directly deposited on the clean porous transport layer (PTL)s: Toray carbon paper and Ni fiber PTL for cathode and anode side, respectively. The electrodes were prepared using an automatic spray coater (Exactacoat by SONO TEK), aiming for a catalyst loading of 1 or 2 mg cm$^{-2}$ and 20% ionomer content for the anode side, and a loading of 0.6 $mg_{Pt}$ cm$^{-2}$ and 25% ionomer content for the cathode side. Before testing the cell, both anode and cathode were soaked in the 1 M KOH electrolyte as a pretreatment.

For the single cell tests, a potentiostatic/galvanostatic workstation (Biologic Science Instruments, BT-815, 15 A max., 10 kHz max.) was used. The measurements were performed in a 5 cm$^2$ cell hardware, with full Nickel serpentine flow-fields on both sides. PTFE gasket were used to make the cell leak-tight: on the cathode, a 250 nm thick foil was used and a 400 nm thick foil was used on the anode side. The anode and cathode sides were fed separately with a 1 M KOH solution at flow rate of 50 mL min$^{-1}$. The cell temperature was set at 55 °C because the AEM-based cells should be operated at 50–60 °C due to their poor chemical stability, which limits operation at high temperatures for a long period.[94–96] The cell was assembled in a cold state, using electrodes (CCS) and membrane which were soaked for 3 h prior to assembly. Then the benchmarking of the single cell measurement protocol started with a cell conditioning step containing 2 h of electrolyte heating at OCV until a steady-state was reached. The break-in step was performed as a galvanostatic sweep with a scan rate of 10 mV s$^{-1}$ between 1.4–2.1 V. The cell was further conditioned for 4 h at a constant current of 1 A cm$^{-2}$.

The polarization curves were recorded four times by setting a constant current value for 1 min from 0.016 to 2 A $cm^{-2}$, with a voltage limit set at 2.1 V. The last potential-current density curve was chosen as the one for evaluation, thus ensuring that, the cell was fully conditioned.

## Supporting Information

Supporting Information is available from the Wiley Online Library or from the author.

## Acknowledgements

The authors acknowledge the Deutsches Elektronen-Synchrotron DESY (Hamburg, Germany), a member of the Helmholtz Association HGF, for the provision of experimental facilities. Parts of this research were carried out at Petra III and the authors would like to thank Edmund Welter and Regina Biller for their assistance in operating the P65 beamline. Beamtime was allocated for proposals I-20200874 and I-20210042. This project has received funding from the Fuel Cells and Hydrogen 2 Joint Undertaking under grant agreement No 875088. This Joint undertaking receives support from the European Union's Horizon 2020 research innovation programme and Hydrogen Europe and Hydrogen Europe Research.

Open access funding enabled and organized by Projekt DEAL.

## Conflict of Interest

The authors declare no conflict of interest.

## Data Availability Statement

The data that support the findings of this study are available from the corresponding author upon reasonable request.

## Keywords

in situ Raman, NiFe-layered double hydroxides, oxygen evolution reaction, water electrolysis, X-ray absorption spectroscopy

Received: March 28, 2022
Revised: June 22, 2022
Published online: July 13, 2022

[1] J. A. Turner, *Science* **2004**, *305*, 972.
[2] F. M. Sapountzi, J. M. Gracia, C. J. Weststrate, H. O. A. Fredriksson, J. W. Niemantsverdriet, *Prog. Energy Combust. Sci.* **2017**, *58*, 1.
[3] K. Zeng, D. Zhang, *Prog. Energy Combust. Sci.* **2010**, *36*, 307.
[4] L. Li, P. Wang, Q. Shao, X. Huang, *Chem. Soc. Rev.* **2020**, *49*, 3072.
[5] B. M. Hunter, H. B. Gray, A. M. Muller, *Chem. Rev.* **2016**, *116*, 14120.
[6] N. T. Suen, S. F. Hung, Q. Quan, N. Zhang, Y. J. Xu, H. M. Chen, *Chem. Soc. Rev.* **2017**, *46*, 337.
[7] W. T. Hong, M. Risch, K. A. Stoerzinger, A. Grimaud, J. Suntivich, Y. Shao-Horn, *Energy Environ. Sci.* **2015**, *8*, 1404.
[8] K. Zeng, X. Zheng, C. Li, J. Yan, J. H. Tian, C. Jin, P. Strasser, R. Yang, *Adv. Funct. Mater.* **2020**, *30*, 2000503.
[9] F. Song, X. Hu, *Nat. Commun.* **2014**, *5*, 4477.
[10] K. Fan, H. Chen, Y. Ji, H. Huang, P. M. Claesson, Q. Daniel, B. Philippe, H. Rensmo, F. Li, Y. Luo, L. Sun, *Nat. Commun.* **2016**, *7*, 11981.
[11] D. Zhou, S. Wang, Y. Jia, X. Xiong, H. Yang, S. Liu, J. Tang, J. Zhang, D. Liu, L. Zheng, Y. Kuang, X. Sun, B. Liu, *Angew. Chem., Int. Ed.* **2019**, *58*, 736.
[12] J. Zhang, L. Yu, Y. Chen, X. F. Lu, S. Gao, X. W. D. Lou, *Adv. Mater.* **2020**, 1906432.
[13] S. Yin, W. Tu, Y. Sheng, Y. Du, M. Kraft, A. Borgna, R. Xu, *Adv. Mater.* **2018**, *30*, 1705106.
[14] X. Zhang, Y. Zhao, Y. Zhao, R. Shi, G. I. N. Waterhouse, T. Zhang, *Adv. Energy Mater.* **2019**, *9*, 1900881.
[15] S. Lee, L. Bai, X. Hu, *Angew Chem Int Ed Engl* **2020**, *59*, 8072.
[16] F. Dionigi, J. Zhu, Z. Zeng, T. Merzdorf, H. Sarodnik, M. Gliech, L. Pan, W. X. Li, J. Greeley, P. Strasser, *Angew. Chem., Int. Ed.* **2021**, *60*, 14446.
[17] H. Liu, J. Zhou, C. Wu, C. Wang, Y. Zhang, D. Liu, Y. Lin, H. Jiang, L. Song, *ACS Sustainable Chem. Eng.* **2018**, *6*, 2911.
[18] Y. Jia, L. Zhang, G. Gao, H. Chen, B. Wang, J. Zhou, M. T. Soo, M. Hong, X. Yan, G. Qian, J. Zou, A. Du, X. Yao, *Adv. Mater.* **2017**, *29*, 1700017.
[19] and G. S. Xiaowen Yu, M. Zhang, W. Yuan, *J. Mater. Chem. A* **2015**, 6921.
[20] Q. Wang, L. Shang, R. Shi, X. Zhang, Y. Zhao, G. I. N. Waterhouse, L.-Z. Wu, C.-H. Tung, T. Zhang, *Adv. Energy Mater.* **2017**, *7*, 1700467.
[21] Q. Xiang, F. Li, W. Chen, Y. Ma, Y. Wu, X. Gu, Y. Qin, P. Tao, C. Song, W. Shang, H. Zhu, T. Deng, J. Wu, *ACS Energy Lett.* **2018**, *3*, 2357.
[22] Z. W. Gao, J. Y. Liu, X. M. Chen, X. L. Zheng, J. Mao, H. Liu, T. Ma, L. Li, W. C. Wang, X. W. Du, *Adv. Mater.* **2019**, *31*, 1804769.
[23] J. Zhang, L. Yu, Y. Chen, X. F. Lu, S. Gao, X. W. D. Lou, *Adv. Mater.* **2020**, 1906432.
[24] L. Yu, J. F. Yang, B. Y. Guan, Y. Lu, X. W. D. Lou, *Angew. Chem., Int. Ed.* **2018**, *57*, 172.
[25] Y. Wang, M. Qiao, Y. Li, S. Wang, *Small* **2018**, *14*, 1800136.
[26] R. Chen, S. F. Hung, D. Zhou, J. Gao, C. Yang, H. Tao, H. B. Yang, L. Zhang, L. Zhang, Q. Xiong, H. M. Chen, B. Liu, *Adv. Mater.* **2019**, *31*, 1903909.
[27] C. C. Pavel, F. Cecconi, C. Emiliani, S. Santiccioli, A. Scaffidi, S. Catanorchi, M. Comotti, *Angew. Chem., Int. Ed.* **2014**, *53*, 1378.
[28] J. R. Varcoe, P. Atanassov, D. R. Dekel, A. M. Herring, M. A. Hickner, P. A. Kohl, A. R. Kucernak, W. E. Mustain, K. Nijmeijer, K. Scott, T. Xu, L. Zhuang, *Energy Environ. Sci.* **2014**, *7*, 3135.
[29] D. Xu, M. B. Stevens, M. R. Cosby, S. Z. Oener, A. M. Smith, L. J. Enman, K. E. Ayers, C. B. Capuano, J. N. Renner, N. Danilovic, Y. Li, H. Wang, Q. Zhang, S. W. Boettcher, *ACS Catal.* **2019**, *9*, 7.
[30] J. J. Kaczur, H. Yang, Z. Liu, S. D. Sajjad, R. I. Masel, *Front. Chem.* **2018**, *6*, 263.
[31] P. Thangavel, M. Ha, S. Kumaraguru, A. Meena, A. N. Singh, A. M. Harzandi, K. S. Kim, *Energy Environ. Sci.* **2020**, *13*, 3447.
[32] H. Koshikawa, H. Murase, T. Hayashi, K. Nakajima, H. Mashiko, S. Shiraishi, Y. Tsuji, *ACS Catal.* **2020**, *10*, 1886.
[33] Y. Han, Z. H. Liu, Z. Yang, Z. Wang, X. Tang, T. Wang, L. Fan, K. Ooi, *Chem. Mater.* **2008**, *20*, 360.
[34] H. Liang, F. Meng, M. Caban-Acevedo, L. Li, A. Forticaux, L. Xiu, Z. Wang, S. Jin, *Nano Lett.* **2015**, *15*, 1421.
[35] Y. Zhao, X. Zhang, X. Jia, G. I. N. Waterhouse, R. Shi, X. Zhang, F. Zhan, Y. Tao, L.-Z. Wu, C.-H. Tung, D. O'Hare, T. Zhang, *Adv. Energy Mater.* **2018**, *8*, 1703585.
[36] S. Klaus, Y. Cai, M. W. Louie, L. Trotochaud, A. T. Bell, *J. Phys. Chem. C* **2015**, *119*, 7243.
[37] B. M. Hunter, J. D. Blakemore, M. Deimund, H. B. Gray, J. R. Winkler, A. M. Müller, *J. Am. Chem. Soc.* **2014**, *136*, 13118.
[38] F. Tang, T. Liu, W. Jiang, L. Gan, *J. Electroanal. Chem.* **2020**, *871*, 114282.
[39] R. L. Frost, M. L. Weier, J. T. Kloprogge, *J. Raman Spectrosc.* **2003**, *34*, 760.
[40] M. C. Biesinger, B. P. Payne, A. P. Grosvenor, L. W. M. Lau, A. R. Gerson, R. S. C. Smart, *Appl. Surf. Sci.* **2011**, *257*, 2717.
[41] A. P. Grosvenor, B. A. Kobe, M. C. Biesinger, N. S. McIntyre, *Surf. Interface Anal.* **2004**, *36*, 1564.

[42] C. Wu, H. Li, Z. Xia, X. Zhang, R. Deng, S. Wang, G. Sun, *ACS Catal.* **2020**, *10*, 11127.
[43] S. Liu, H. Zhang, E. Hu, T. Zhu, C. Zhou, Y. Huang, M. Ling, X. Gao, Z. Lin, *J. Mater. Chem. A* **2021**, *9*, 23697.
[44] T. S. Munonde, H. Zheng, P. N. Nomngongo, *Ultrason. Sonochem.* **2019**, *59*, 104716.
[45] D. Zhou, S. Wang, Y. Jia, X. Xiong, H. Yang, S. Liu, J. Tang, J. Zhang, D. Liu, L. Zheng, Y. Kuang, X. Sun, B. Liu, *Angew. Chem., Int. Ed.* **2019**, *58*, 736.
[46] P. Li, X. Duan, Y. Kuang, Y. Li, G. Zhang, W. Liu, X. Sun, *Adv. Energy Mater.* **2018**, *8*, 1703341.
[47] B. M. Hunter, W. Hieringer, J. R. Winkler, H. B. Gray, A. M. Müller, *Energy Environ. Sci.* **2016**, *9*, 1734.
[48] B. Grégoire, C. Ruby, C. Carteret, *J. Chem. Soc. Dalt. Trans.* **2013**, *42*, 15687.
[49] B. Grégoire, C. Ruby, C. Carteret, *Cryst. Growth Des.* **2012**, *12*, 4324.
[50] M. Steimecke, G. Seiffarth, M. Bron, *Anal. Chem.* **2017**, *89*, 10679.
[51] C. C. McCrory, S. Jung, J. C. Peters, T. F. Jaramillo, *J. Am. Chem. Soc.* **2013**, *135*, 16977.
[52] M. K. Bates, Q. Jia, H. Doan, W. Liang, S. Mukerjee, *ACS Catal.* **2015**, *6*, 155.
[53] L. Trotochaud, S. L. Young, J. K. Ranney, S. W. Boettcher, *J. Am. Chem. Soc.* **2014**, *136*, 6744.
[54] B. Zhang, L. Wang, Z. Cao, S. M. Kozlov, F. P. G. De Arquer, C. T. Dinh, J. Li, Z. Wang, X. Zheng, L. Zhang, Y. Wen, O. Voznyy, R. Comin, P. De Luna, T. Regier, W. Bi, E. E. Alp, C. Pao, L. Zheng, Y. Hu, Y. Ji, Y. Li, Y. Zhang, L. Cavallo, H. Peng, E. H. Sargent, *Nat. Catal.* **2020**, 985.
[55] X. Zheng, B. Zhang, P. De Luna, Y. Liang, R. Comin, O. Voznyy, L. Han, F. P. Garcia de Arquer, M. Liu, C. T. Dinh, T. Regier, J. J. Dynes, S. He, H. L. Xin, H. Peng, D. Prendergast, X. Du, E. H. Sargent, *Nat. Chem.* **2018**, *10*, 149.
[56] Z. K. Goldsmith, A. K. Harshan, J. B. Gerken, M. Vörös, G. Galli, S. S. Stahl, S. Hammes-Schiffer, *Proc. Natl. Acad. Sci. USA* **2017**, *114*, 3050.
[57] N. Li, D. K. Bediako, R. G. Hadt, D. Hayes, T. J. Kempa, F. von Cube, D. C. Bell, L. X. Chen, D. G. Nocera, *Proc. Natl. Acad. Sci* **2017**, *114*, 1486.
[58] L. Francas, S. Corby, S. Selim, D. Lee, C. A. Mesa, R. Godin, E. Pastor, I. E. L. Stephens, K. S. Choi, J. R. Durrant, *Nat. Commun.* **2019**, *10*, 5208.
[59] F.-Y. Chen, Z.-Y. Wu, Z. Adler, H. Wang, *Joule* **2021**, 1.
[60] S. Cherevko, A. R. Zeradjanin, G. P. Keeley, K. J. J. Mayrhofer, *J. Electrochem. Soc.* **2014**, *161*, H822.
[61] Z. Qiu, C. W. Tai, G. A. Niklasson, T. Edvinsson, *Energy Environ. Sci.* **2019**, *12*, 572.
[62] M. W. Louie, A. T. Bell, *J. Am. Chem. Soc.* **2013**, *135*, 12329.
[63] B. J. Trzesniewski, O. Diaz-Morales, D. A. Vermaas, A. Longo, W. Bras, M. T. M. Koper, W. A. Smith, *J. Am. Chem. Soc.* **2015**, *137*, 15112.
[64] F. Dionigi, P. Strasser, *Adv. Energy Mater.* **2016**, 6.
[65] J. Mohammed-Ibrahim, *J. Power Sources* **2019**.
[66] D. Friebel, M. W. Louie, M. Bajdich, K. E. Sanwald, Y. Cai, A. M. Wise, M. J. Cheng, D. Sokaras, T. C. Weng, R. Alonso-Mori, R. C. Davis, J. R. Bargar, J. K. Norskov, A. Nilsson, A. T. Bell, *J. Am. Chem. Soc.* **2015**, *137*, 1305.
[67] M. B. Stevens, C. D. M. Trang, L. J. Enman, J. Deng, S. W. Boettcher, *J. Am. Chem. Soc.* **2017**, *139*, 11361.
[68] H. Xiao, H. Shin, W. A. Goddard, *Proc. Natl. Acad. Sci* **2018**, *115*, 5872.
[69] F. Dionigi, Z. Zeng, I. Sinev, T. Merzdorf, S. Deshpande, M. B. Lopez, S. Kunze, I. Zegkinoglou, H. Sarodnik, D. Fan, A. Bergmann, J. Drnec, J. F. de Araujo, M. Gliech, D. Teschner, J. Zhu, W. X. Li, J. Greeley, B. R. Cuenya, P. Strasser, *Nat. Commun.* **2020**, *11*, 2522.
[70] J. Huang, Y. Li, Y. Zhang, G. Rao, C. Wu, Y. Hu, X. Wang, R. Lu, Y. Li, J. Xiong, *Angew. Chem., Int. Ed.* **2019**, *58*, 17458.
[71] A. Y. Faid, A. O. Barnett, F. Seland, S. Sunde, *Catalysts* **2018**, *8*, 614.
[72] A. Lim, H. juhn Kim, D. Henkensmeier, S. Jong Yoo, J. Young Kim, S. Young Lee, Y. E. Sung, J. H. Jang, H. S. Park, *J. Ind. Eng. Chem.* **2019**, *76*, 410.
[73] J. E. Park, S. Y. Kang, S. H. Oh, J. K. Kim, M. S. Lim, C. Y. Ahn, Y. H. Cho, Y. E. Sung, *Electrochim. Acta* **2019**, *295*, 99.
[74] S. C. Zignani, M. Lo Faro, S. Trocino, A. S. Aricò, *Energies* **2020**, *13*, 1720.
[75] I. V. Pushkareva, A. S. Pushkarev, S. A. Grigoriev, P. Modisha, D. G. Bessarabov, *Int. J. Hydrogen Energy* **2020**, *45*, 26070.
[76] M. K. Cho, H. Y. Park, H. J. Lee, H. J. Kim, A. Lim, D. Henkensmeier, S. J. Yoo, J. Y. Kim, S. Y. Lee, H. S. Park, J. H. Jang, *J. Power Sources* **2018**, *382*, 22.
[77] Z. Liu, S. Dawar Sajjad, Y. Gao, H. Yang, J. J. Kaczur, R. I. Masel, *Inorg. Chem. Front.* **2017**, 29661.
[78] J. Xiao, A. M. Oliveira, L. Wang, Y. Zhao, T. Wang, J. Wang, B. P. Setzler, Y. Yan, *ACS Catal.* **2021**, *11*, 264.
[79] A. Loh, X. Li, O. O. Taiwo, F. Tariq, N. P. Brandon, P. Wang, K. Xu, B. Wang, *Int. J. Hydrogen Energy* **2020**, *45*, 24232.
[80] X. Li, F. C. Walsh, D. Pletcher, *Phys. Chem. Chem. Phys.* **2011**, *13*, 1162.
[81] E. López-Fernández, J. Gil-Rostra, J. P. Espinós, A. R. González-Elipe, A. De Lucas Consuegra, F. Yubero, *ACS Catal.* **2020**, *10*, 6159.
[82] P. Z. Chen, X. L. Hu, *Adv. Energy Mater.* **2020**, *10*, 2002285.
[83] F. Zhang, H. Zhang, M. Salla, N. Qin, M. Gao, Y. Ji, S. Huang, S. Wu, R. Zhang, Z. Lu, Q. Wang, *J. Am. Chem. Soc.* **2021**, *143*, 223.
[84] E. Ruska-centre, E. Ruska-centre, E. Ruska-centre, *J. large-scale Res. Facil.* **2016**, *41*, 3.
[85] E. Welter, R. Chernikov, M. Herrmann, R. Nemausat, *AIP Conf. Proc.* **2019**, *2054*, 040002.
[86] B. Ravel, M. Newville, *J. Synchrotron Radiat.* **2005**, *12*, 537.
[87] B. Ravel, *J. Synchrotron Radiat.* **2001**, *8*, 314.
[88] F. J. Scott, S. Mukerjee, D. E. Ramaker, *J. Electrochem. Soc.* **2007**, *154*, A396.
[89] S. Calvin, *XAFS for Everyone*, CRC Press, **2013**.
[90] F. J. Pérez-Alonso, C. Adán, S. Rojas, M. A. Peña, J. L. G. Fierro, *Int. J. Hydrogen Energy* **2014**, *39*, 5204.
[91] A. Y. Faid, A. O. Barnett, F. Seland, S. Sunde, *Electrochim. Acta* **2020**, 137040.
[92] A. Y. Faid, A. O. Barnett, F. Seland, S. Sunde, *Electrochim. Acta* **2021**, 371.
[93] S. Niu, S. Li, Y. Du, X. Han, P. Xu, *How to Reliably Report the Overpotential of an Electrocatalyst 5*, American Chemical Society, **2020**, pp. 1083.
[94] K. F. L. Hagesteijn, S. Jiang, B. P. Ladewig, *J. Mater. Sci.* **2018**, *53*, 11131.
[95] H. A. Miller, K. Bouzek, J. Hnat, S. Loos, C. I. Bernäcker, T. Weißgärber, L. Röntzsch, J. Meier-Haack, *Sustain. Energy Fuels* **2020**, *4*, 2114.
[96] L. Xia, W. Jiang, H. Hartmann, J. Mayer, W. Lehnert, M. Shviro, *ACS Appl. Mater. Interfaces* **2022**.